On the influence of fabrication methods and materials for mRNA-LNP production: from size and morphology to internal structure and mRNA delivery performance in vitro and in vivo

Bi, D.D.; Wilhelmy, C.; Unthan, D.; Keil, I.S.; Zhao, B.N.; Kolb, B.; ... ; Zhang, H.Y.

RESEARCH ARTICLE

ADVANCED HEALTHCARE MATERIALS
www.advhealthmat.de

On the Influence of Fabrication Methods and Materials for mRNA-LNP Production: From Size and Morphology to Internal Structure and mRNA Delivery Performance In Vitro and In Vivo

Dongdong Bi, Christoph Wilhelmy, Dennis Unthan, Isabell Sofia Keil, Bonan Zhao, Bastian Kolb, Roman I. Koning, Melissa A. Graewert, Bert Wouters, Raphaël Zwier, Jeroen Bussmann, Thomas Hankemeier, Mustafa Diken, Heinrich Haas, Peter Langguth, Matthias Barz,* and Heyang Zhang**

Lipid nanoparticle (LNP) remains the most advanced platform for messenger RNA (mRNA) delivery. To date, mRNA LNPs synthesis is mostly performed by mixing lipids and mRNA with microfluidics. In this study, a cost-effective microfluidic setup for synthesizing mRNA LNPs is developed. It allows to fine-tune the LNPs characteristics without compromising LNP properties. It is compared with a commercial device (NanoAssemblr) and ethanol injection and the influence of manufacturing conditions on the performance of mRNA LNPs is investigated. LNPs prepared by ethanol injection exhibit broader size distributions and more inhomogeneous internal structure (e.g., bleb-like substructures), while other LNPs show uniform structure with dense cores. Small angel X-ray scattering (SAXS) data indicate a tighter interaction between mRNA and lipids within LNPs synthesized by custom device, compared to LNPs produced by NanoAssemblr. Interestingly, the better transfection efficiency of polysarcosine (pSar)-modified LNPs correlates with a higher surface roughness than that of PEGylated ones. The manufacturing approach, however, shows modest influence on mRNA expression in vivo. In summary, the home-developed cost-effective microfluidic device can synthesize LNPs and represents a potent alternative to NanoAssemblr. The preparation methods show notable effect on LNPs' structure but a minor influence on mRNA delivery in vitro and in vivo.

1. Introduction

Messenger ribonucleic acid (mRNA) technologies have emerged as an innovative and efficient approach for the development of new drugs with a wide range of applications, such as regenerative medicine, cancer treatment, gene editing, and vaccine development.[1] As exemplified by FDA approval of delivering small interfering RNA (siRNA, Onpattro) and antigen mRNA (Comirnaty, Spikevax) drugs, lipid nanoparticles (LNPs) are so far among the most clinically advanced platforms. State-of-the-art LNPs are the assembled nanoparticles composed of four lipid components, namely (ionizable) cationic lipid (e.g., Dlin-MC3-DMA, ALC-0315, SM-102), phospholipid (e.g., DSPC, DOPE), cholesterol, polyethylene glycol (PEG)-lipid (e.g., DMG-PEG2k, ALC-0159).[2] An increasing number of studies have shown that the functional delivery of mRNA by an LNP greatly depends on the inclusion of mRNA into the lipid matrix. Libraries of chemically

D. Bi, D. Unthan, B. Zhao, B. Wouters, J. Bussmann, T. Hankemeier, M. Barz, H. Zhang
Leiden Academic Centre for Drug Research (LACDR)
Leiden University
Einsteinweg 55, Leiden 2333 CC, The Netherlands
E-mail: m.barz@lacdr.leidenuniv.nl; h.zhang@lacdr.leidenuniv.nl

The ORCID identification number(s) for the author(s) of this article can be found under https://doi.org/10.1002/adhm.202401252

DOI: 10.1002/adhm.202401252

C. Wilhelmy, B. Kolb, H. Haas, P. Langguth
Department of Biopharmaceutics and Pharmaceutical Technology
Johannes Gutenberg University Mainz
55128 Mainz, Germany
E-mail: langguth@uni-mainz.de

I. S. Keil, M. Diken
TRON-Translational Oncology at the University Medical Center of Johannes Gutenberg University GmbH
55131 Mainz, Germany

R. I. Koning
Electron Microscopy Facility
Department of Cell and Chemical Biology
Leiden University Medical Center
Leiden 2300 RC, The Netherlands

distinct lipids, therefore, have been created to achieve more efficient, specific, and safe mRNA delivery. The advent of novel synthetic, particularly ionizable lipids has accelerated the clinical translation of RNA drugs.[3] In addition, novel shielding lipids, including PEG-lipid alternative, are important for the future success of RNA drugs.[4,5] In this respect, polysarcosine (pSar)-lipids, have been developed.[6] As a polymer, pSar is based on the endogenous amino acid sarcosine (methyl glycine), and can be synthesized by controlled living ring-opening polymerization of the corresponding *N*-carboxyanhydride, possessing comparable main chain flexibility and solubility in buffer.[7] Most importantly, pSar displayed PEG-like properties (e.g., stealth-like properties in vivo) and enables the synthesis of nanoparticles without detectable protein corona.[8–16] We have reported the monoalkyl pSar-lipids and bisalkyl pSar-lipids.[17,18] These pSar-lipids have been applied to lipid formulations, with substantially reduced immunogenicity, cytokine levels, or complement activation of such nanoparticles compared with PEGylated nanoparticles.[6,19–22] Notably, the synthesis of pSar-modified nanoparticles can be performed by the same techniques known for established stealth lipids.[23,24] Therefore, such pSar-lipids are one of the most promising alternatives to established polymer-lipid conjugates.

It is well-established that characteristics of mRNA LNPs, such as lipid composition, size, surface charge, and stability, play a vital role in biodistribution and therapeutic potency, and thus can be optimized to achieve organ or cell-specific delivery and maximal efficacy.[25] Production techniques, ideally featuring low cost, ease of use, small sample size, precise control, high reproducibility, and fast preparation, are therefore required. Microfluidics are a robust, scalable, and reproducible approach to generate LNPs by assembling lipids and mRNA payload into nanoparticles by on-chip technologies. By fine-tuning the process parameters of mixing organic and aqueous phases, LNPs with precisely defined properties can be reproducibly and efficiently synthesized. Of note, microfluidics can produce LNPs on laboratory as well as on industrial scale.[26] With those advantages over traditional lipid-film hydration, microfluidics have emerged as a gold standard for preclinical LNPs production.[27]

Within the microfluidic device, LNPs form at the aqueous-to-ethanol interface by diffusion-based ethanol dilution. When lipid-dissolving ethanol is rapidly diluted with RNA-containing buffer to a critical ethanol concentration, small and homogeneous LNPs form at the liquid–liquid interface.[27] In addition to the flow rate condition, the geometry of the micromixer including the mixing cycles and dimension of the channel greatly influences the size of LNPs and their stability.[28,29] To precisely control the physical properties of LNPs (e.g., size, morphology, structure), various micromixer systems have been constructed and evaluated, such as T-, Y-shaped, chaotic, and baffle mixers. For example, NanoAssemblr has been extensively used to produce RNA LNPs (20–200 nm). The NanoAssemblr Benchtop cartridge employs a chaotic mixer with a staggered herringbone that induces homogeneous mixing in the microchannel by chaotic convection and thus increases the size controllability of LNPs compared to T- or Y-shaped micromixers at ambient flow rates. Such a chaotic mixer structure, however, is preferable for mixing solutions at low flow rates as the mixing performance is reduced under high-flow-rate conditions.[30] Recently, the NanoAssemblr Ignite system with a planar asymmetric split-and-recombine micromixer and a toroidal mixer has been released.[31] By using the Dean vortex, this new microchannel structure is suitable for high-flow-rate conditions, thus reaching scalability without the parallelization of multiple chips. Very interestingly, iLiNP, a microfluidic device with a simple baffle structure and microchannel fluid dynamics relative to the chaotic mixer, has been reported to precisely produce LNPs with a 10 nm size distribution.[32] A layered flow of ethanol and buffer solution is maintained in the microchannel, and ethanol is rapidly diluted by secondary flow at the baffle structures. The iLiNP device shows preferable ethanol dilution performance at high-flow rates.[33,34] The development of novel microfluidic mixing devices may offer enhanced versatility and affordability for small-scale development of nanoparticles with tailored properties. Nevertheless, it is unclear to which extent the microfluidic production method influences the final performance of mRNA LNPs. Since the development of microfluidics for RNA LNPs formulation is in its relative infancy, far less is known about the correlation between the internal structure of mRNA LNPs and their physicochemical properties and biological performance.

In this present study, we developed and optimized a microfluidic device for synthesizing mRNA LNPs with different shielding lipopolymers. The microfluidic chamber is based on the chaotic mixer, which is cost-effective and can be reused more than 40 times. Its performance was evaluated by comparing the mRNA LNPs prepared by the commercially available NanoAssemblr and the traditional ethanol injection, in terms of size, size distribution, surface charge, morphology, internal structure, storage stability, in vitro transgene expression, as well as biodistribution and protein production in zebrafish embryos after intravenous injection.

2. Experimental Section

2.1. Materials

1,2-Dioleoyl-*sn*-glycero-3-phosphorylethanolamine (DOPE) and methoxypolyethylengly-coloxy(2000)-*N*,*N*-ditetradecylacetamide (ALC-0159) were purchased from Avanti Polar Lipids (Alabaster, AL). Ionizable lipid heptratriaconta-6,9,28,31-tetraen-19-yl-4-(dimethylamino)butanoate (DLin-MC3-DMA) was bought from MedChemExpress (Monmouth Junction, NJ). Cholesterol was ordered from Merck (Darmstadt, Germany). BA_{C14}-$pSar_{36}$-Azide (pSar) was synthesized in the Barz Lab as previously described (Leiden, The Netherlands).[24] All lipid stocks were stored at −20 °C in lyophilized form or dissolved in ethanol. Milli-Q water

M. A. Graewert
European Molecular Biology Laboratory (EMBL) Hamburg Outstation
c/o DESY
22607 Hamburg, Germany
R. Zwier
Leiden Institute of Physics Research
Leiden University
Einsteinweg 55, Leiden 2333 CC, The Netherlands
M. Barz
Department of Dermatology
University Medical Center of the Johannes Gutenberg University Mainz
Langenbeckstraße 1, 55131 Mainz, Germany

was prepared using a MILLI-Q Reference A^+ system. Water was used at a resistivity of 18.2 MΩ cm^{-1} and total organic carbon < 5 ppm. CleanCap enhanced green fluorescent protein (EGFP) mRNA was bought from Tebubio (Heerhugowaard, The Netherlands). Cy5-labeled luciferase mRNA was provided by TRON/Biontech SE (Mainz, Germany). The Quant-it RiboGreen RNA Assay Kit was ordered from Thermo Fisher Scientific (Bleiswijk, The Netherlands). Borosilicate glass microneedles with filament was bought from Sutter Instruments (BF100-78-10, USA). HEPES, chloroform, tricaine, agarose, Tris-base, ethylenediaminetetraacetic acid (EDTA), and D-(+)-glucose were purchased from Sigma-Aldrich (Zwijndrecht, The Netherlands). Bovine serum albumin, trypsin/EDTA, and Dulbecco's Modified Eagle's Medium/F12 (DMEM/F12) were purchased from Thermo Fisher Scientific (Bleiswijk, The Netherlands). RPMI1640, L-glutamine, PEN-STREP (10 000 U mL^{-1} penicillin, 10 000 U mL^{-1} streptomycin), and DPBS (without Ca^{2+} or Mg^{2+}) were bought from Lonza Bioscience (Verviers, Belgium). Fetal bovine serum was purchased from SERANA (Brandenburg, Germany). The other reagents and solvents were purchased from Sigma Aldrich (Zwijndrecht, The Netherlands).

2.2. Methods

2.2.1. Preparation of mRNA LNPs

Lipid stock solutions containing DLin-MC3-DMA, DOPE, cholesterol, and stealth lipid (ALC-0159 or pSar) at a molar ratio of 40/10/48/2 were mixed in ethanol at a total lipid concentration of 15 mM. In the preparation of LNPs, the lipid concentration was diluted to 3.75 mM and the final mRNA LNPs formulation was concentrated to 15 mM (5500 g, 10 min). The mRNA stock solution (0.133 mg mL^{-1}) was diluted with citrate buffer (50 mM, pH 5). Lipids and mRNA were mixed using different techniques at N/P ratio 5. To visualize the distribution of mRNA LNPs, Cy5-labeled luciferase mRNA and EGFP encoding mRNA were mixed at a w/w ratio of 1:3 before being loaded into LNPs. LNPs were prepared using the NanoAssembl Ignite platform (NanoAssemblr), Precision Nano-Systems Inc., Vancouver, BC, Canada), customized microfluidic device, and ethanol injection as described below.

mRNA LNPs Prepared by NanoAssemblr: Briefly, the lipids mixture was combined with an acidic buffer of 50 mM sodium citrate (pH 5.0) containing mRNA at a flow rate ratio of 1:3 (3 and 9 mL min^{-1}, respectively) using NanoAssemblr Ignite instrument with NxGen cartridges (Precision Nanosystems, Vancouver, BC, Canada).

mRNA LNPs Prepared by Customized Microfluidic Device: Lipids mixture in ethanol and mRNA in citrate buffer (50 mM, pH 5.0) were loaded into 500 µL and 1 mL Hamilton syringes (Giarmata, Timis County, Romania), respectively, and mixed within a customized microfluidic chamber under defined flow rate conditions.

mRNA LNPs Prepared by Ethanol Injection: LNP formulations were prepared using the previously reported ethanol injection method.[22] In brief, the mRNA/aqueous was pipetted onto the lipid/ethanol, followed by an immediate vortex for 10 s.

All formulations were dialyzed against DPBS (1 x, pH 7.4) overnight in Pur-A-Lyzer 12–14 kDa dialysis cassettes (Sigma-Aldrich, Zwijndrecht, The Netherlands) overnight at 4 °C. Afterward, the formulations were concentrated using Amicon Ultra 100 K Centrifuge Filter (Merck KGaA, Darmstadt, Germany) and centrifuged at 5 500 g for 10 min at 4 °C before use.

2.2.2. Characterization of mRNA LNPs

Dynamic Light Scattering (DLS): The Zetasizer Ultra (Malvern, Worcestershire, UK) was employed to determine the hydrodynamic diameter (intensity distribution) and ζ potential of mRNA LNPs. This analysis was conducted in HEPES buffer (10 mM, pH 7.4) at a final total lipid concentration of 100 µM. The encapsulation efficiency of LNPs was tested by Quant-it RiboGreen RNA Assay Kit following the manufacturing protocol.

Cryogenic Electron Microscopy (cryoEM): Electron microscopy support grids (R2/2, Quantifoil, Germany) were glow discharged in air at 0.2 mbar, 25 mA, and 30 s, using a Pelco Easiglow. Onto the glow discharged grids, 3 µL of sample was placed and subsequently blotted away for 3 s using filter paper (Whatman no.4) at 85%–95% humidity using a Leica EM GP. The grid was directly plunged into liquid-ethane/propane (1:2) kept at −196 °C. Grids were clipped into autogrids, placed into a cassette, and transferred into a Talos Arctica cryo-electron microscope (Thermo Fisher Scientific). Images were recorded using EPU software (Thermo Fisher Scientific) in multigrid mode with a K3 direct electron detector (Gatan) in counting mode and ZLP imaging. Images were recorded in movie mode at a magnification of 15 000 x (corresponding to a pixel size of 0.55 nm at specimen level), a defocus of −5 µm, and an electron dose of ≈4 e/A2/s with 8 s exposure time (corresponding to a total dose of 35 e/A2). Using this magnification/pixel size and electron dose the full 2 µm hole is visible in one image the vesicle bilayer (at 4 nm) can be discerned. Movies were aligned using MotionCorr2 and converted to tiff using EMAN2.[35]

Small Angle X-Ray Scattering: SAXS data were collected at the P12 BioSAXS beamline of the European Molecular Biology Laboratory (EMBL) at the PETRAIII synchrotron, DESY Hamburg (Germany).[36] The measurements were performed at an X-ray energy of 10 keV (wavelength 0.124 nm) and a sample-detector distance of 6 m (q-range 0.01–2.20 nm^{-1}). Utilizing the BioSAXS sample changer, 30 µL of the sample was transferred to a quartz capillary mounted in vacuum.[37] 2D scattering patterns were collected by a Pilatus 6 M detector with an exposure time of 0.095 s. For raw data processing, SASFLOW and ATSAS software (EMBL Hamburg, Hamburg, Germany) were used.[36,38,39] Averaged data were transferred to QTIPlot 1.0.1 software (IONDEV, Bucuresti, Romania) for further data analysis. For buffer subtraction same procedure was executed with DPBS buffer (1 x, pH 7.4, without Ca^{2+} or Mg^{2+}) as a sample. The scattering profile of the buffer was subtracted from the respective sample profiles after proper scaling.

All data are given as scattering internsity $I(q)$ presented as a function of the momentum transfer calculated according to Equation (1)

$$q = \frac{4\pi}{\lambda} \sin(\theta) \quad (1)$$

where λ is the X-ray wavelength and 2 Θ is the scattering angle. The correlation of extrapolated scattering intensity at $q = 0$ I_0, which is a measure for the total scattering intensity, and the particle volume V is described in Equation (2), where n is the number density of particles and $\Delta\rho$ is the contrast of the scattering material[40]

$$I_0 = n \cdot V^2 \cdot (\Delta\rho)^2 \tag{2}$$

SAXS data for the investigated q-range include the form factor of the single nanoparticles, which is determined by overall size, shape and surface of the LNPs, as well as Bragg reflections derived from mRNA-lipid interactions within the LNPs.

For investigation of overall particle size, Guinier plots were used according to Equation (2), to obtain the radius of gyration R_g[41]

$$\ln I(q) = \ln I_0 - \frac{R_g^2}{3} q^2 \tag{3}$$

For spherical particles the average radius can be calculated from the R_g by

$$r = \sqrt{\frac{5}{3}}\, R_g \tag{4}$$

Additional information can be revealed by analyzing the intensity decay of the whole SAXS profile using the power law as shown in the equation below, which gives information about fractal dimensionality and the packing compactness of the particles

$$I(q) = I_0 \cdot q^{-x} \tag{5}$$

For particles with smooth surfaces, a decay indicated by the so-called Porod exponent x with values between 3 and 4 can be observed, while slopes with lower decay in the range of 2–3 is observed for particles with surface fractals.[42]

For investigation of internal structure properties, Lorentzian fit functionality was used for peak fitting of the Bragg refelctions in each SAXS pattern, as given in

$$\mathrm{I}(q) = I_0 + \frac{2A}{\pi} \cdot \frac{\mathrm{w}}{4 \cdot \left(q - q_c\right)^2 + w^2} \tag{6}$$

With I_0 being the baseline intensity, A the peak area, w the peak width (FWHM), and q_c the center position of the peak. The peak position can be used to calculate the repeat distance of the scattering moiety (so called d-spacing) for lamellar systems using the Bragg equation[43]

$$d = \frac{2\pi}{q_c} \tag{7}$$

Additional conclusions can be gained from the peak width w, which gives information about the correlation length inside the ordered arrays. Here, the correlation length scales reciprocally with the peak width, meaning that a narrow peak is an indicator for a long correlation length. A generally accepted model for liquid crystalline structures describes the correlation length ξ, which is defined as the distance at which the positional correlation decays to the value $1/e$[44]

$$\xi = \frac{2}{\mathrm{w}} \tag{8}$$

Multiangle DLS Analysis: Cylindrical quartz cuvettes (Hellma, Muhlheim, Germany) were meticulously cleaned using dust-free distilled acetone and placed within a dust-free flow box. Solutions were filtered into the cuvettes through Millex-GV filters with a pore size of 0.22 µm. DLS measurements were conducted at 20 °C using a Uniphase He/Ne Laser (22.5 mW output power at λ = 632.8 nm) and an ALV/CGS-8F SLS/DLS 5022F goniometer with eight simultaneously operating ALV 7004 correlators and eight ALV/High QEAPD avalanche photodiode detectors. Multiangle DLS measurements were analyzed by using ALVStat 4.31 software (ALV, Germany) under 26°, 58°, 90°, and 122°.

2.2.3. In Vitro and In Vivo Biological Performance of mRNA LNPs

Cell Culture: HepG2 cells were cultured in DMEM/F12 with 10% Fetal Bovine Serum (FBS), 2 mM L-glutamine, and 100 µg mL^{-1} penicillin/streptomycin at 37 °C, 5.0% CO_2. Cells with 80%–90% confluency were detached from the bottom of the flask with 0.25% trypsin/EDTA. Jurkat T cells were cultured in RPMI1640 medium supplemented with 10% FBS, 100 µg mL^{-1} penicillin/streptomycin and 2 mM L-glutamine, and maintained in a humidified atmosphere of 37 °C, 5.0% CO_2. The culture medium was renewed every 2–4 days. For all in vitro tests, HepG2 cells were seeded in 96-well F-bottom plates (Greiner Bio-one, Alphen aan den Rijn, The Netherlands) at a density of 15 000 cells per well. Jurkat T cells were seeded in 96-well U-bottom plates (Greiner Bio-one, Alphen aan den Rijn, The Netherlands) at a density of 40 000 cells per well. Cells were incubated at 37 °C, 5.0% CO_2 one day before treatment.

2.2.4. In Vitro Transfection

LNPs containing EGFP mRNA were utilized to study the protein expression in HepG2 cells and Jurkat T cells, respectively. In each well, 20 µL mRNA LNPs (containing 0.2 µg EGFP mRNA) was transferred to the cells cultured in fresh culture medium with a final volume of 200 µL. After 24 h incubation at 37 °C, 5.0% CO_2, HepG2 cells were rinsed with DPBS twice, trypsinized and collected by centrifugation at 500 g for 5 min, while Jurkat T cell pellet was harvested after washing with DPBS twice and subsequent centrifugation at 500 g, 5 min. 200 µL flow buffer (1% bovine serum albumin, 0.1% NaN_3, in DPBS) was added to each well to resuspend cell pellets for measurements by flow cytometry (Cytoflex, Beckman Colter, Woerden, The Netherlands), to quantify protein expression.

2.2.5. Zebrafish Husbandry and Strains

Zebrafish (Danio rerio) were used for studies in compliance with the regulations and norms for animal care set forth by the

European Convention for the Protection of Vertebrate Animals (ECPVA) and the local animal welfare council of Leiden University. Fertilized eggs were collected and raised at 28 °C in egg water (60 µg mL^{-1} Instant Ocean sea salts) and embryos were anesthetized and embedded in 0.4% agarose (with 0.01% tricaine) in egg water before microinjection.

2.2.6. Zebrafish Injection and Imaging

A micropipette puller (P-97, Sutter Instruments) was utilized to prepare needles using borosilicate capillaries with filaments. To visualize the biodistribution and protein production of mRNA LNPs, 20 ABTL (wild-type) zebrafish embryos (2.5 dpf) were embedded in 0.4% agarose gel containing tricaine and injected with 2 nL LNPs containing 75 pg EGFP mRNA and 25 pg Cy5 luciferase mRNA using an Eppendorf Femtojet pump. Embryos that had been successfully injected were then taken out of the agarose and cultured at 28 °C. Embryos were re-embedded in confocal dishes and photographed using Leica TCS SP8 confocal microscopy at 3 h postinjection (hpi). A 40 x water immersion objective (HCX APO L) and a 10 x air objective (HCX PL FLUOTAR) were used to take Z-stack images. All stacks and sessions used the same laser intensity, gain, and offset settings. Regarding the quantification, the whole-body images of six ABTL embryos were taken using a 10 x air objective to quantify the transfection effect of mRNA LNPs. The Fiji Image J (1.53 t, Java 1.8.0_322) was used to process the images and the mean fluorescent intensity of EGFP in each embryo was quantified. Mean gray values were recorded under the threshold from 15 to 255.

2.2.7. Statistical Analysis

To evaluate statistical differences between experimental groups in this study multiple *t*-test was performed in DLS data and two-way ANOVA was performed in GraphPad Prism 9 for in vitro test. Values of $p < 0.05$ were considered statistically significant, and asterisks indicate statistical significance: $*p < 0.05$; $**p < 0.01$; $***p < 0.001$, $****p < 0.0001$. Two-way ANOVA followed by Tukey's multiple comparisons test in Graphpad was used for the in vivo study.

3. Results and Discussion

3.1. Fabrication of a Chaotic Mixer for the Preparation of LNPs

As an initial step in this work, we aimed to establish the synthesis of mRNA LNPs using a customized microfluidic device. Here, LNPs comprised of ionizable lipid DLin-MC3-DMA bearing an amine group that is positively charged at pH 5.0, the phospholipid DOPE, cholesterol, and shielding lipid, either PEGylated lipid ALC-0159 or polypeptide-based lipopolymer pSar.[24,45] The hydrophilic PEG or pSar coats the surface of LNPs and thus prevents aggregation of LNPs during production, storage as well as upon injection in vivo.[21,46] For the formulation, when mRNA in aqueous buffer with a low pH is rapidly mixed with lipids in the organic phase, such as ethanol, LNPs form spontaneously due to hydrophobic and electrostatic interactions between the positively charged ionizable lipid and the anionic mRNA. The structure of the generated mRNA LNPs has been thoroughly investigated by a multitude of methods, in particular, cryoEM and SAXS measurements. Despite some differences in the detailed description, all studies point to compact nanoparticles with low internal organization, where the RNA is embedded in an excess of lipidic material.[47–50]

To date, the most widely used microfluidic system to generate mRNA LNPs is the NanoAssemblr, which has the drawback of high cost due to one-time use of microfluidic chip. Since it is reported that chaotic mixer structures enhance the controllability of LNP size, we developed a chaotic mixer to mix mRNA with lipids.[27] The design of the microfluidic chip is depicted in **Figure 1** and can be easy copied. To reach precise control over mixing speed, a long mixing length is required to fully mix two fluids at high flow speeds. The mixer was fabricated from Topas microscopy slides (75 × 25 mm) made of thermoplastic polymer (cyclic olefin copolymer), which is nonpolar, amorphous, and chemical resistant. It also has a very low permeability for water vapor and a low capacity for the absorption of water. The mixer was designed as 46.80 mm in length and 7.73 mm for the length of 1 mixer section. The staggered herringbone micromixers were utilized to enhance mixing by advection rather than diffusion. It consists of a rectangular channel with embossed grooves on the bottom, where these grooves have an asymmetrical V-shape (note that the peak of the V is not in the middle of the geometry's width) and 6 asymmetric grooves followed by a group of 6 reverse asymmetric grooves,[51] as illustrated in Figure 1A,B. The chaotic mixer can be enclosed within a plastic holder with the assistance of a metal bracket to ensure a tight fit (Figure 1C,D). Plastic tubing can be used to connect the syringes on the pump (Fusion 100-X High precision syringe pump) to the chamber and to collect the samples. In addition, this cost-effective chip can be used more than 40 times without notable variation in terms of size, surface charge, and encapsulation efficiency of LNPs.

3.2. Higher Total Flow Rate and Flow Rate Ratio Produced Small-Sized mRNA LNPs

The quality of LNPs is heavily affected by the production procedure.[27] Typically, modulating mixing parameters, like total flow rate (TFR) and flow rate ratio (FRR) of aqueous and ethanol phase, changes the dynamics of the nanoprecipitation reaction and solubility of the lipid components, thus controlling size and dispersity of mRNA LNPs. Here, mRNA LNPs composed of DLin-MC3-DMA, DOPE, cholesterol, and PEG- and pSar-lipids at a molar ratio of 40/10/48/2 were prepared at varying flow conditions, as shown in **Table 1**. Initially, we kept the flow rate ratio (FRR) as 3:1 (mRNA in aqueous: lipids in ethanol) and varied the total flow rate (TFR) at 0.8, 1.2, and 1.6 mL min^{-1}. In general, all the generated mRNA LNPs were negatively charged, around −11 mV. This is inconsistent with previous reports that ionizable lipid MC3 has a pKa of 6.2–6.4 and thus the surface of mRNA LNPs has an almost neutral charge in PBS buffer (pH 7.4).[52] While only slight changes were found in the hydrodynamic diameter of mRNA LNPs, ranging from 120 nm (0.8 mL min^{-1}) to

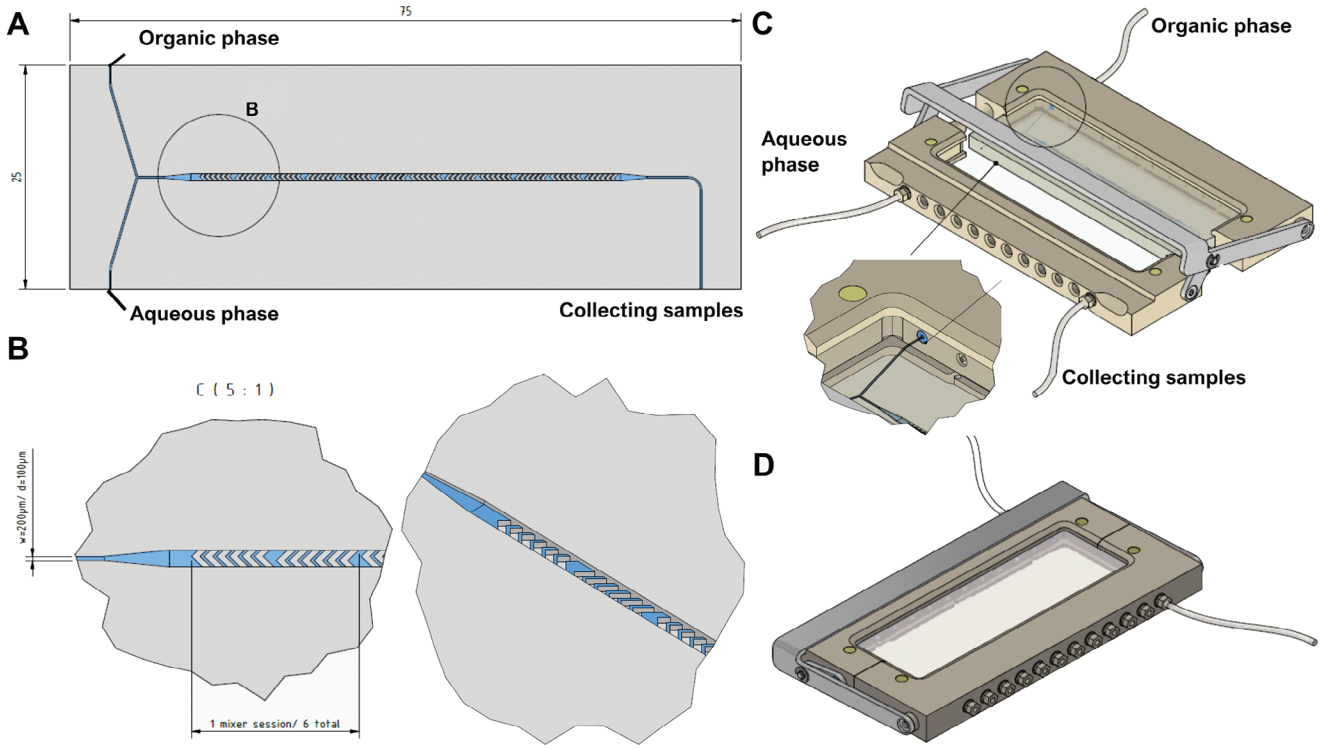

Figure 1. Scheme of chaotic mixer structure within the customized microfluidic device. A) The organic phase and aqueous phase in two channels can be mixed in the chaotic mixer chamber. B) Zoomed view of 1 unit grooves. C) Scheme of microfluidic chip holder with plastic input and output tubes to prepare and collect samples. D) Closed state of microfluidic chip holder.

150 nm (1.2 mL min^{-1}), the polydispersity index (PDI) showed a notable decrease with increasing TFR. Although it was reported that increasing the total volumetric flow rate during formulation increases mixing efficacy and decreases the time scale of particle formation, resulting in smaller particles, we did not see a notable decrease in the particle size of mRNA LNPs by increasing the TFR during mixing.[53] Decreasing the TFR broadens the distribution due to increased particle residence time at lower flow rates, allowing further aggregation to occur and larger particles to form at the outlet, thus an overall increase in PDI is observed. Therefore, higher TFRs are preferable. Moreover, the encapsulation efficiency (EE%), as determined by the RiboGreen assay, increased up to 90% when the TFR increased, indicating the fraction of accessible mRNA is very low for high TFRs. With respect to size, PDI, and EE%, the TFR was kept at 1.6 mL min^{-1} to generate mRNA LNPs in further studies.

Next, we explored the FRR for mRNA LNP production. In general, LNPs became smaller with increased FRR, where aggregates

Table 1. Optimization of CD prepared pSar-LNPs ($n = 6$).

Optimizing total flow rate (TFR)						
mRNA: lipid flow rates [mL min^{-1}]	FRR	TFR [mL min^{-1}]	Size [nm]	PDI	ζ potential [mV]	EE [%]
0.6:0.2	3	0.8	122.5 ± 10.6	0.25 ± 0.04	−10.1 ± 1.4	66.1 ± 2.0
0.9:0.3	3	1.2	149.2 ± 30.4	0.19 ± 0.07	−11.3 ± 0.1	72.4 ± 3.3
1.2:0.4	3	1.6	132.9 ± 6.5	0.10 ± 0.04[a)]	−11.3 ± 0.7	88.8 ± 1.5
Optimizing flow rate ratio (FRR)						
mRNA: lipid flow rates [mL min^{-1}]	FRR	TFR [mL min^{-1}]	Size [nm]	PDI	ζ potential [mV]	EE [%]
0.8:0.8	1	1.6	Aggregation	—	—	—
1.1:0.5	2.2	1.6	153.4 ± 19.8	0.14 ± 0.04	−12.6 ± 1.6	66.7 ± 4.2
1.2:0.4	3	1.6	129.3 ± 3.8	0.17 ± 0.03	−17.5 ± 2.1	91.8 ± 9.4

[a)] Indicated that $p < 0.5$ compared to the mRNA LNPs synthesized at flow rate of 0.6:0.2.

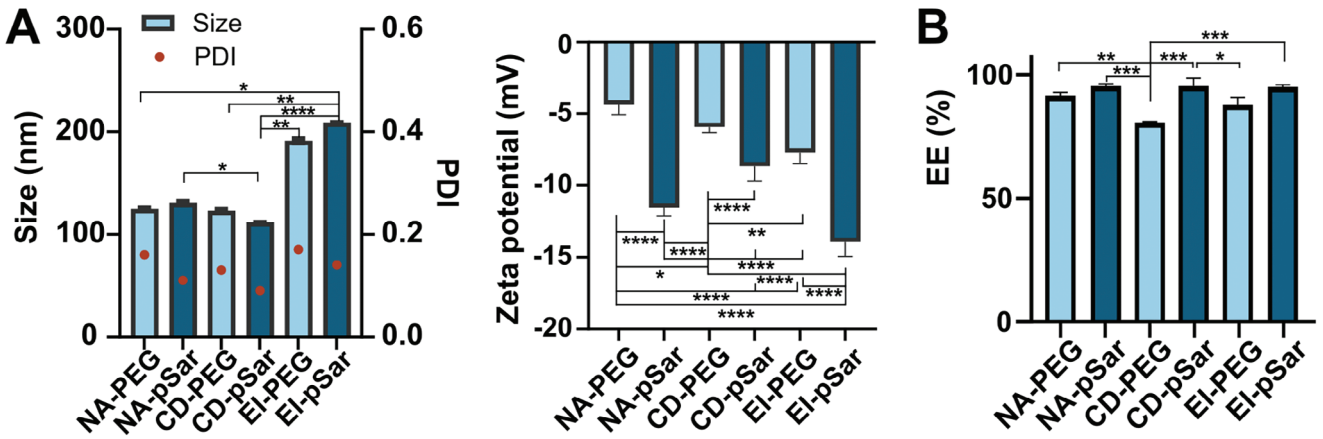

Figure 2. Characterization and stability of PEG/pSar LNPs prepared by NA, CD, and EI methods. A) Size, PDI, and surface charge of all LNPs were measured by DLS ($n = 6$). B) Encapsulation rate of all LNPs. Data are presented as mean ± SD. The formulated mRNA LNPs were named as manufacturing approach-shielding lipopolymers. *$p < 0.05$; **$p < 0.01$; ***$p < 0.001$, ****$p < 0.0001$.

were detected when FRR was 1, while a particle size of 130 nm could be reached with the FRR at 3. These findings align with previously reported literature, indicating that smaller LNPs can be achieved when the ethanol phase is rapidly diluted.[27] Conversely, decreasing the FRR increases ethanol concentration at the mixing interface, thus increasing lipid solubility and lengthening particle formation time, allowing for particle growth. Moreover, when FRR increased from 2.2 to 3, EE% of mRNA LNPs was improved from 67% to 90%. To sum up, both TFR and FRR affect the physicochemical properties of mRNA LNPs substantially. The higher TFR and FRR, the more defined mRNA LNPs can be produced. Considering that i) the higher total flow volumetric rate leads to the higher pressure within the microchannel, and ii) increasing either TFR or FRR generated small-sized LNPs, we synthesized mRNA LNPs at TFR of 1.6 mL min^{-1} and FRR of 3 in the next studies. More importantly, this device showed high reproducibility of size distribution, surface charge, and EE (%) of mRNA LNPs from batch to batch, as shown in the independent runs with the same settings in Table 1.

3.3. Small-Sized, Defined mRNA LNPs were More Stable During Storage

To evaluate the home-developed microfluidic device (CD), mRNA LNPs were synthesized using the commonly used NanoAssemblr (NA) and traditional method of ethanol injection (EI). We aim to understand whether different LNP fabrication methods and materials affect the internal structure and performance of LNPs. Compared with NanoAssemblr, our custom device is more cost-effective and reusable. However the downside is that our pump cannot achieve the high flow rate of the NanoAssemblr, which will be improved in further studies. As an alternative to pSar, PEGylated lipid ALC-0159 was incorporated into mRNA LNPs to investigate its impact on the physicochemical and biological performance of formulated mRNA LNPs (Table S1, Supporting Information).

For the characterization of mRNA LNPs, we examined the size, PDI, and ζ potential of formulated mRNA LNPs (**Figure 2**). By using the microfluidic device, either NA or CD, mRNA LNPs were comparable in terms of size (around 130 nm) and PDI (below 0.2), while the simple mixing of lipids and mRNA (ethanol injection) resulted in larger nanoparticles (up to 200 nm). These findings indicate that the use of higher flow rates and microfluidic channel geometry optimized for those flow conditions can decrease the LNP size. Since the lipid concentration was kept at 3.75 mM for mRNA LNPs synthesis, the difference in size of LNPs produced by microfluidics and EI may attribute to the different mixing conditions. When ethanol was instantaneously diluted within the microchannel, the intermediate planar fragments had little time to grow before closing into vesicles, resulting in smaller particles. When ethanol was diluted slowly by manual mixing, pockets of high ethanol concentration developed, thus favoring stabilization and growth of intermediate fragments that lead to large-sized LNPs.[54] All mRNA LNPs were slightly negatively charged with ζ potential between −5 and −15 mV, and over 80% of mRNA was protected from accessibility to dissolved dyes by the LNPs under all conditions (RiboGreen assay).

Further, we studied the storage stability of mRNA LNPs at 4 °C over 3 months, in terms of size and PDI (Figure S1, Supporting Information). Again, mRNA LNPs produced using microfluidics remained stable, were 100–150 nm in size with PDI below 0.25, and no significant difference was found within 3 months. Using CD, pSar-containing mRNA LNPs were slightly smaller than their PEGylated counterparts but slightly larger than the analogues prepared using NA. Overall, the smallest LNPs with PDIs around 0.1 and EE(%) around 90% can be achieved with the customized microfluidic chip as described above.

In contrast, the size of PEGylated mRNA LNPs gradually increased (180.3 ± 1.2 nm at 1 week vs 199.4 ± 3.3 nm at 3 months), indicating that EI-prepared LNPs may be less stable compared to their counterparts. With the same manufacturing approach of EI, the increase in size of pSar-decorated LNPs from 209.2 ± 0.3 to 213.1 ± 4.4 nm was not as evident as for the PEGylated LNPs, suggesting that pSar can increase the stability of EI-synthesized mRNA LNPs.

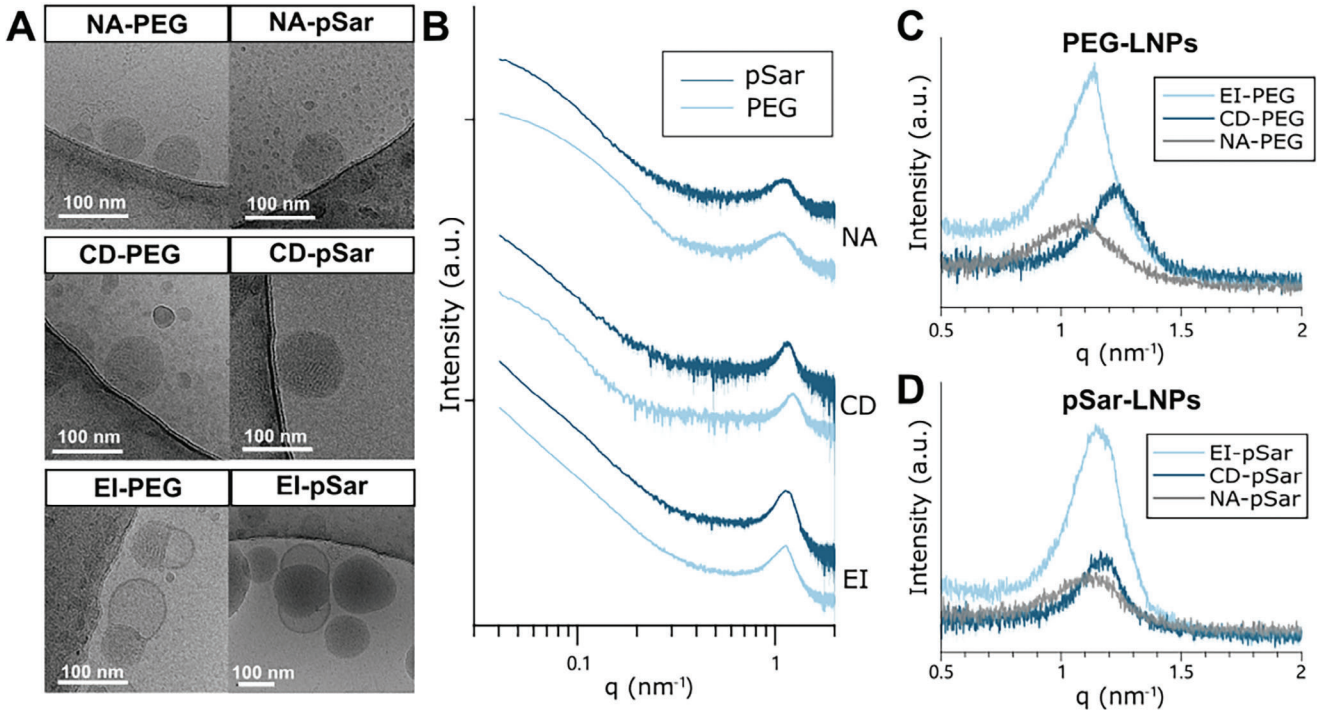

Figure 3. A) Representative CryoEM images of PEG-containing mRNA LNPs (left pane) and pSar-containing mRNA LNPs (right panel) prepared by NA (top panel), CD (middle panel), and EI methods (bottom panel). B) SAXS pattern of PEGylated mRNA LNPs (dark blue) or pSar-containing LNPs (light blue) prepared by NA (top panel), CD (middle panel), and EI (bottom panel). C,D) Bragg peak characteristics of C) PEG-containing mRNA LNPs and D) pSar-containing mRNA LNPs using different manufacturing methods.

3.4. pSar-LNPs have Higher Surface Roughness than PEG-LNPs

To analyze the structure of the mRNA LNPs synthesized by different methods (i.e., NA, CD, and EI), cryoEM imaging was performed, as shown in **Figure** 3A. Microfluidics produced smaller particles while EI generated larger particles (≈200 nm). For small-sized particles prepared by microfluidics, either NA or CD, cryoEM images exhibited a similar feature of ordered electron-dense cores, whereas large-sized particles produced by EI display a different characteristic. The majority of EI-PEG LNPs exhibited an electron-dense core, accompanied by a large aqueous bleb compartment (associated lipid vesicle that was devoid of RNA) situated on one side indicating phase separation of lipid components. Only a minority of them had the typical dense core shape. It is noteworthy that Wang et al. observed similar bleb-shaped structures from siRNA LNPs synthesized by EI.[55] On the other hand, most EI-pSar LNPs shared a similar morphology with NA and CD-prepared LNPs, which had large dense cores. Notably, some of the EI-pSar LNPs exhibited more than one aqueous bleb structure around the dense core. Our observation suggests that also the choice of shielding lipid, i.e., pSar and PEG, can influence the morphological characteristics of LNPs when utilizing the EI method, but this influence is not observed when using higher-speed mixer methods such as NA and CD. Bleb-like substructures are supposed to be derived from lipid components forming a bilayer due to the phase segregation of phospholipids like DSPC, which are not favorably compatible with the inverted hexagonal phase in the electron-dense core.[47] Also the choice of the manufacturing buffer and its ionic strength influences the tendency to formation of blebs on LNP formulations, where these formulations showed an enhanced transfection efficacy compared to nonbleb LNPs.[56] In this experiment, DOPE was used as a phospholipid, which is due to its unsaturated lipid chains being more compatible with this organization and thus does not tend to form subphases.[57] Nevertheless, the formation of bleb-like structures can be observed in cryoEM images, which may be explained by the slower ethanol dilution within manual mixing, leading to more heterogeneous particle formation. Since PEG-lipids reside on the surface of the LNPs, molar fraction also determines particle size as well as the tendency to build blebs.[58] The observation of bleb-like structures as a matter of the manufacturing method highlights that not only the choice of materials but also the formulation process has a tremendous influence on the particle structure. Exchanging PEG with pSar may only slightly affect LNP microstructure and size as visible in Figures 2 and 3A. A multiangle DLS analysis was also performed, and all LNPs exhibited a slight angle dependency (Figure S2, Supporting Information), which may relate to moderate dispersity and the complex structure.

To further investigate differences in the internal structure of LNPs, small angle X-ray scattering (SAXS) measurements were conducted. Figure 3B displays the results of batch SAXS measurements, showcasing the scattering patterns of each sample. These patterns are dominated by a broad peak around 1 nm^{-1}, reflecting the internal organization of particles. The low q range was analyzed using Guinier plots to determine the radius of gyration (R_g). Consistent with DLS and cryoEM findings, NA-produced formulations exhibit the lowest R_g, while

Table 2. SAXS data analysis of PEG- or pSar-containing mRNA LNPs manufactured by NA, CD, and EI.

Name	R_g [nm]	Average calculated radius [nm]	Porod exponent	*d*-spacing [nm]	Correlation length [nm]
NA-PEG	25.8	33.3	3.7 ± 0.1	6.0 ± 0.1	4.7 ± 0.1
NA-pSar	33.3	43.0	3.5 ± 0.1	5.7 ± 0.1	5.5 ± 0.2
CD-PEG	40.1	51.7	3.3 ± 0.1	5.2 ± 0.1	7.1 ± 0.2
CD-pSar	50.6	65.3	3.1 ± 0.1	5.5 ± 0.1	8.0 ± 0.2
EI-PEG	64.9	83.8	3.2 ± 0.1	5.6 ± 0.1	9.1 ± 0.2
EI-pSar	69.9	90.3	3.0 ± 0.1	5.5 ± 0.1	8.3 ± 0.1

LNPs manufactured by EI have a R_g approximately twice as large as those made with microfluidic devices. Assuming spherical particles, the average radius of LNPs can be calculated, yielding comparable results to DLS experiments, with R_g/R_h ratios close to 0.78, which is indicative for uniform spheres (**Table 2**; and Table S2, Supporting Information).

We further analyzed the low q region from 0.08 to 0.25 nm^{-1} by the power law (Equation (5)), to determine the fractal dimension of the LNPs (Figure S3, Supporting Information). Smooth surfaces lead to an exponent, x, of 4 (Porod law), while lower numbers imply increased surface roughness or fractal dimension. As Table 2 displays, pSar-modified LNPs have lower value of Porod exponents than the PEGylated counterparts, regardless of the manufacturing method. In our previous work we found that compared to PEGylated LNPs, the increase of fractal dimension in the presence of pSar is accompanied by higher biological activity.[22]

In addition, surface properties strongly depend on the manufacturing method. NA-LNPs tend to show a Porod exponent of around 3.5 or bigger, indicating smooth surfaces. Conversely, the Porod region decay of CD- and EI-LNPs is closer to 3, suggesting surface fractals. Especially for EI-manufactured LNPs it is well accompanied with findings from cryo-EM, where bleb like structures were observed. It was found that the LNPs' surface was less polar with increasing particle size, and changes in LNPs' size led to changes in the mRNA organization and LNPs' surface properties.[59] High fractal dimensions and irregular surfaces are hypothesized to be beneficial for cell transfection by facilitating membrane rupture within endosomal uptake processes.[60]

The Bragg peak, resulting from internal organization of the LNPs provides insights into packing density of the cargo within the lipid vehicle. Figure 3C,D demonstrates that the peak characteristics differ among LNPs generated by various manufacturing methods. The Bragg reflection area is larger for EI-LNPs compared to the microfluidic produced LNPs, which can be explained by the larger particle size. Accordingly, the extrapolated scattering intensity at $q = 0$, obtained from the Guinier plot, is higher for the EI-LNPs. The particles manufactured by EI exhibit larger diameters and, consequently, higher volumes per particle.[40,61] The peak observed in the EI-LNPs (Figure 3C,D, dark blue), is characterized by two subpeaks, indicating subphases in internal organization, while the microfluidic methods display a single peak. The additional front peak at 0.85 nm^{-1} along with the main peak at 1.1 nm^{-1} contributes to the total scattering pattern of the formulation (Table S3, Supporting Information). This highlights the ability of microfluidic manufacturing processes in producing well-defined nanoparticles without lipidic substructures, such as the observed blebs in cryoEM.

Furthermore, both peak position and width differ among all the LNPs synthesized using various manufacturing methods. NA-produced particles yield broad peaks with peak maxima around 1.05 nm^{-1}. Compared to NA-LNPs, CD-LNPs showed sharper peaks shifted toward higher *q*. This indicates a tighter internal packing of the mRNA, resulting in lower d-spacing. Comparing the correlation length derived from peak width between the two microfluidic mixing procedures, a higher long-range order of mRNA-lipid interactions was observed. However, the level of long-range order remains relatively low in the range of the *d*-spacing, as it is typical for mRNA-LNP systems. Interestingly, despite lower mixing speeds in synthesizing CD-LNPs, which might suggest a looser mRNA packing density, the chaotic mixing chamber in the customized device enables closer lipid-mRNA interaction and thus tighter packing. To check if these internal features can be derived at different flow conditions also using the NA device, LNP formulations manufactured with variable TFRs were investigated with DLS and SAXS (Figure S4, Supporting Information). Independent of TFR, all LNPs showed *d*-spacing values around 6 nm, as for the primary investigated NA samples. Interestingly, the low flow rate at 1 mL min^{-1} resulted in LNPs with an average diameter of around 250 nm, while increasing the TFR decreased LNP size (Table S4, Supporting Information). These results indicate that for NA, the liquid flow rate also influences overall particle size more than the internal organization. Dense packing properties have recently been proposed as beneficial for transfection in specific cell types, such as human peripheral blood mononuclear cells.[22] Moreover, the nonmicrofluidic ethanol injection protocol results in a lower packing density and relatively higher correlation length compared to the NA protocol. Differences in peak behavior were also observed when comparing formulations with different stealth moieties. For NA- and EI-manufactured LNPs, slightly denser RNA-lipid interactions were obtained with pSar-shielded LNPs, while in the customized microfluidic setting the pSar formulation showed slightly higher *d*-spacing compared to its PEG analogs.

Analyzing the scattering profile of the different formulations revealed distinct variations in both the overall particle appearance and internal organization. The microfluidic NA protocol successfully generated smoothly spherical nanoparticles with a discrete diameter below 100 nm, exhibiting a low degree of internal organization. On the other hand, manual EI approaches produced larger LNPs with irregular surfaces and lipidic substructures. In comparison to the well-established and widely used NA

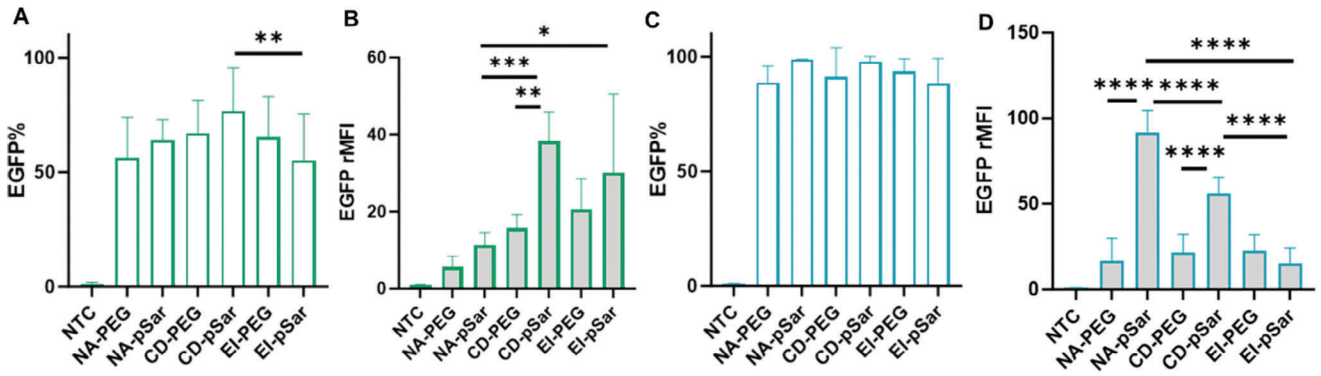

Figure 4. In vitro transfection efficiency of EGFP mRNA LNPs after being exposed to A,B) HepG2 cells and C,D) Jurkat T cells for 24 h, respectively. The transfection efficiency was represented as fraction of A,C) EGFP-positive cells (EGFP%) and B,D) relative mean fluorescence intensity (EGFP rMFI) based on untreated cells (NTC). All the experiments were performed on three independent days ($n = 9$). Data are presented as mean ± SD. *$p < 0.05$; **$p < 0.01$; ***$p < 0.001$, ****$p < 0.0001$.

microfluidic process, the customized microfluidic device presented here can produce LNPs with comparable particle sizes, but with slightly different surface and internal order characteristics. We failed to achieve these characteristics with the NA while changing experimental settings. These differences are hard to distinguish with standard quality control measures, but still can play an important role for therapeutic efficacy. The presence of more irregular surfaces and higher packing density of the mRNA cargo in CD formulations may be potentially advantageous for cellular transfection,[22] as it can play a crucial role for endosomal escape mechanisms. The higher fractal dimension of CD-manufactured LNPs can be explained by the lower TFR and therefore slightly slower ethanol dilution leading to differences in primary particle formation. This is also observable for NA-LNPs with slower TFRs as displayed in Table S4 (Supporting Information). Conversely, the higher packing density cannot be explained by this, since it was not reproducible in NA with lower TFRs. Here the geometry of the microfluidic mixers seems to be one of the driving forces for differences in the mRNA-lipid complex. Further investigation with different lipid compositions and mixer geometries could help to elucidate this phenomenon. Additionally, these LNPs showed lower diameters and reduced polydispersity compared to manually produced EI-LNPs. Thus, the development of the novel microfluidic approach enables the production of robustly monodisperse nanoparticles with uniform structural features without altering the lipid composition.

3.5. 5 pSar-mRNA LNPs Outperformed PEG-mRNA LNPs in Transfection In Vitro

Next, we evaluated the biological performance of mRNA LNPs on two different cell lines, the human liver cancer cell line HepG2 and the human immortalized T lymphocyte cell line derived from an acute T cell leukemia (Jurkat T cells), respectively. After being exposed to the formulated EGFP mRNA LNPs for 24 h, cells were collected and examined by flow cytometry for transfection efficiency. As shown in **Figure** 4A,B, EGFP production was detected in more than 50% of HepG2 cells. Notably, a robust EGFP expression was detected in the cells treated with pSar-modified mRNA LNPs, with a significant difference in the EGFP(%) compared to the counterparts prepared by EI (**, $p = 0.005$). As well, EGFP relative mean fluorescence intensity (rMFI) derived from cells exposed to CD-pSar LNPs was significantly higher than the PEGylated mRNA LNPs generated by CD (**, $p = 0.0021$) and pSar-LNPs generated by NA (***, $p = 0.0001$), respectively. In addition, a dramatic difference in EGFP rMFI was found in the cells exposed to pSar-LNPs synthesized using NA and EI (*, $p = 0.0193$).

In Jurkat T cells, over 90% of cells expressing EGFP were detected, without any significant difference in EGFP-positive cells (%) among all formulations tested in this study (Figure 4C,D). Likely, microfluidic-generated pSar-LNPs resulted in more robust EGFP production than that of PEGylated LNPs using the same manufacturing approach, with a significant difference in EGFP rMFI (****, $p < 0.0001$ for NA; ****, $p < 0.0001$ for CD). Among the different production methods, NA-pSar mRNA LNPs led to the most efficient protein production, which is 1.6-fold and 6.1-fold rMFI compared to pSar-LNPs generated by CD or EI. In contrast to the findings in HepG2 cells, pSar-LNPs produced by EI led to the lowest EGFP rMFI (15.2 ± 9.0), followed by pSar-LNPs produced by CD (56.3 ± 9.3). Surprisingly, EGFP rMFI measured in the cells exposed to PEGylated mRNA LNPs was around 20, independent of the manufacturing method.

Overall, the transfection efficiency of mRNA LNPs is cell line-dependent, where large particles led to more robust protein expression in adherent HepG2 cells, while small-sized particles showed more efficient mRNA delivery in suspended Jurkat T cells. This may be due to the partial aggregation of EI-LNPs in the culture medium and thus the cellular internalization was achieved by difference in endocytosis compared to more stable and small-sized particles. Meanwhile, the shielding lipid is of significance to transfection efficiency, particularly in Jurkat T cells. In accordance with our previous work, pSar as stealth moieties affected the LNPs differently, by changing the surface morphology toward higher roughness. Although stability in serum/culture medium is comparable, the elevated surface roughness of the pSar-LNPs compared to those with PEG, may foster interaction with the oppositely charged endosomal membrane upon cellular uptake and protonation of ionizable lipids, resulting in the facilitated rupture of the membrane and the release of the mRNA into the cytosol.[22,62] Therefore, a higher transfection efficiency was

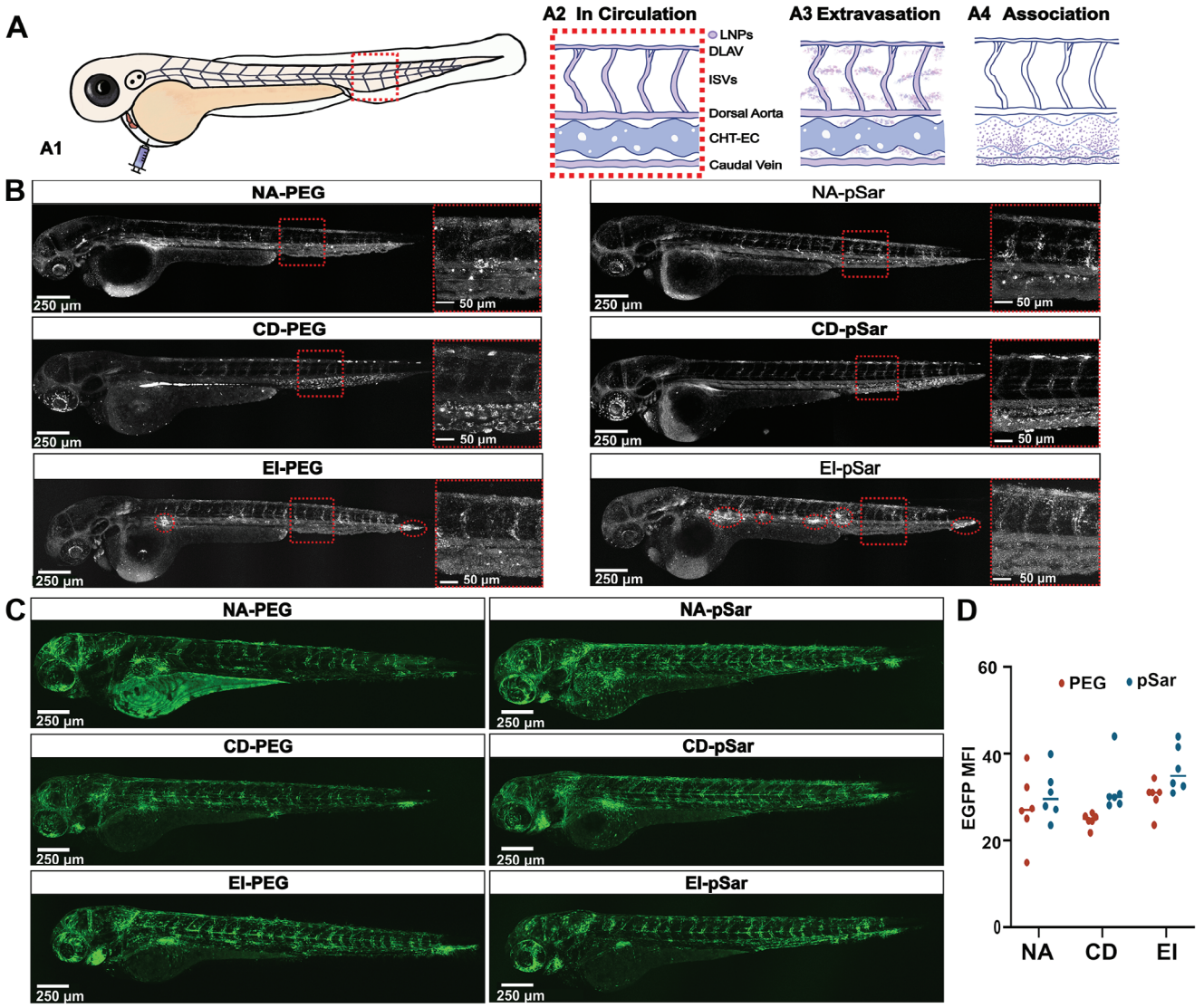

Figure 5. In vivo behavior of NA-PEG/Psar, CD-PEG/pSar, and EI-PEG/Psar LNPs. All LNPs with mixed mRNA (2 nL, EGFP:Cy5 mRNA = 3:1 w/w, 75 pg EGFP mRNA) were injected into zebrafish embryos. A) Scheme for LNPs microinjection into the Duct of Cuvier of 2.5 dpf zebrafish embryos. Zoomed-in tissue-level images depict LNP distributions within the indicated red boxes. Blood vessels are represented by blue lines, while LNPs are shown in purple. CHT-EC: Caudal Hematopoietic Tissue Endothelial Cells, DLAV: Dorsal Longitudinal Anastomotic Vessel, ISV: Intersegmental Vessel. A2) LNPs are located within the lumen of blood vessels, indicating a free circulation pattern. A3) LNPs extravasate from the blood vessels. A4) LNPs are associated with caudal endothelial cells. B) Biodistribution was observed at 3 hpi, red circles show aggregation of LNPs, and red boxes show tissue-level images. C) Transfection effects were observed at 24 hpi. D) Quantification of transfection effect in the whole fish view images ($n = 6$).The scale of the whole fish is 250 μm, and the enlarged tail images in the red square is 50 μm.

observed. In addition, the impact of the manufacturing method or the size of LNPs on the in vitro transfection efficiency is more notable in Jurkat T cells than in HepG2 cells.

3.6. NA, CD, and EI-LNPs Display Robust Transfection Effects In Vivo

To evaluate the different mRNA LNPs in a more complex cellular environment, we loaded Cy5 labeled luciferase mRNA and EGFP mRNA into LNPs, and intravenously injected these LNPs into zebrafish embryos at 2.5 days postfertilization (dpf). The scheme of microinjection in zebrafish embryos and the biodistribution pattern of LNPs are shown in **Figure** 5A. We first examined the biodistribution of mRNA by capturing the Cy5 fluorescence signal (shown in gray) under a confocal microscope at 3 hour postinjection (hpi), as presented in Figure 5B. All LNPs were freely circulating in the blood vessel lumens, owing to the shielding lipid and neutral surface of the LNPs, and began to associate with caudal endothelial cells over time, which have a function similar to that of liver scavenger endothelial cells.[63] Vascular extravasation (leakage of LNPs from blood vessels into the embryonic muscle tissue) was also evident for all LNPs, as it is a common phenomenon for neutral nanoparticles.[63] However, EI-prepared

PEG- and pSar-LNPs display a tendency to form aggregate in circulation, suggesting that EI-LNPs exhibit in general lower stability compared to NA- and CD-LNPs, which is in line with the particle inhomogeneity observed in cryo-EM.

The transfection efficiency was assessed by visualizing the expression of EGFP (represented in green) in Figure 5C. Across all LNPs, the pattern of EGFP mRNA transfection closely mirrored their biodistribution, with notable green fluorescence in blood vessels and muscle tissue. This observation strongly suggests the successful delivery, uptake, and subsequent release of functional mRNA within the cytoplasm in embryos. There was, however, no notable distinction observed among the LNPs based on the representative images. To further assess their in vivo transfection efficacy at the whole zebrafish embryo level, we captured images of six embryos and quantified the mean EGFP fluorescence intensity using ImageJ (Figure 5D). Although the EGFP mean fluorescence intensity (MFI) value for CD-PEG LNPs (24.7 ± 1.6) was relatively lower than that of the other groups (CD-pSar: 34.2 ± 6.0), this variance was still not statistically significant ($p = 0.08$). Interestingly, EI-prepared LNPs and microfluidic-prepared LNPs achieved comparable transfection effects, and the aggregation of EI-LNPs did not considerably influence their transfection effects in muscle and endothelial cells. The bleb structures found in EI-LNPs may play a role in enhancing transfection efficacy in vivo, as previously observed LNPs containing similar blebs.[56]

The transfection after LNP storage of 3 months of at 4 °C was also examined in zebrafish embryos (Figure S5, Supporting Information). The confocal microscope settings used for taking GFP expression images were kept consistent throughout all experiments in this study. NA-PEG, NA-pSar, and EI-pSar exhibited a visible decrease in green fluorescence compared to their freshly prepared analogs. This observation indicates that the transfection efficacy of LNPs decreased after 3 months in solution even though there were only minor changes in the size and PDI of LNPs (Figure 2C). The quantification data exhibited an average of EGFP MFI in the three groups is around 20 (Figure S6, Supporting Information), which is 1.5–2 times lower than that of fresh samples.

4. Conclusion

In this study, we fabricated a customized microfluidic device to synthesize mRNA LNPs. Using this home-developed device, the flow rate of the aqueous-to-ethanol ratio had a notable influence on the size, PDI, and entrapment of mRNA LNPs, while the influence of the total flow rate was modest. Further, the influence of different manufacturing methods (microfluidics and ethanol injection) and different shielding lipids (PEG and pSar) on the morphology, structure, biodistribution, and transfection performance of mRNA LNPs was investigated. With the microfluidic manufacturing approach, the customized microfluidic device was compared to the established commercially available NanoAssemblr. In general, microfluidics generated small-sized, more homogenous, and stable mRNA LNPs compared to the LNPs prepared by ethanol injection. Moreover, the microfluidic-produced mRNA LNPs exhibited the ordered electron-dense cores, whereas ethanol injection-produced LNPs displayed a large aqueous bleb compartment (associated lipid vesicle that was devoid of RNA) around the dense cores. PEGylated and pSar-formulated LNPs were comparable in size, dispersity and internal morphology, while with pSar the surface roughness was systematically higher, which was found to be correlated with higher in vitro transfection effect. Interestingly, SAXS data indicated LNPs generated by custom microfluidics presented more rough surfaces and higher packing density of the mRNA cargo than LNPs produced by commercial device. This highlights the importance of investigations on structural properties, since the differences were not properly detectable with standard quality control measures as DLS, but can have influence on therapeutic potency. Although the transfection efficiency of LNPs prepared by different methods was comparable, ethanol injection-generated LNPs showed aggregation in vivo after systemic injection. In summary, the findings indicate, that by using a customized microfluidic device, LNPs with comparable quality with respect to those obtained from a commercial device can be obtained more cost-effectively, and that microfluidics allows for better control over physicochemical characteristics of mRNA LNPs than ethanol injection. In conclusion, our findings highlight the potential of custom microfluidic devices and materials for mRNA LNPs synthesis to modulate and improve the structure and final performance of mRNA LNPs. The correlation between the internal structure of mRNA LNPs and their physicochemical properties and biological performance can provide valuable insights for mRNA LNPs optimization and production.

Supporting Information

Supporting Information is available from the Wiley Online Library or from the author.

Acknowledgements

D.B. would like to acknowledge the financial support from the China Scholarship Council (No. 201906210053). C.W. and P.L. would like to acknowledge the financial support from CRC 1066 founded by the Deutsche Forschungsgemeinschaft. M.B. acknowledged support by the CRC1066-2/−3 (Project B12) for the development of polysarcosine lipids and formulations thereof.

Conflict of Interest

M.B. and H.H. are co-inventors on PCT/EP2018/076633. M.B. is scientifc advisory board member of Curapath (Paterna, Spain). The other authors do not have any conflicts of interest.

Author Contributions

D.B. and C.W. contributed equally to this work. Conceptualization: P.L., M.B., H.Z.; Data curation: D.B., C.W., H.Z.; Formal analysis: D.B., C.W., H.Z.; Funding acquisition: M.D., P.L., M.B.; Investigation: D.B., C.W., D.U., I.S.K., B.Z, B.K, RI.K., M.A.G., R.Z, T.H, M.D, H.H; Methodology: H.Z., D.B, C.W, B.W, J.B; Project administration: P.L., M.B., H.Z; Resources: P.L.; M.B.; Supervision: P.L., M.B., H.Z; Validation; Visualization: D.B., C.W., H.Z.; Writing – original draft: D.B., C.W., H.Z.; and Writing – review & editing H.Z, M,B, P.L.

Data Availability Statement

The data that support the findings of this study are available in the supplementary material of this article.

Keywords

LNP internal structure, microfluidics, mRNA delivery, PEGylated lipids, polysarcosine

Received: April 15, 2024
Revised: June 13, 2024
Published online: June 25, 2024

[1] N. Al Fayez, M. S. Nassar, A. A. Alshehri, M. K. Alnefaie, F. A. Almughem, B. Y. Alshehri, A. O. Alawad, E. A. Tawfik, *Pharmaceutics* **2023**, *15*, 1972.
[2] M. Jeong, Y. Lee, J. Park, H. Jung, H. Lee, *Adv. Drug Delivery Rev.* **2023**, 114990.
[3] K. Lam, P. Schreiner, A. Leung, P. Stainton, S. Reid, E. Yaworski, P. Lutwyche, J. Heyes, *Adv. Mater.* **2023**, *35*, 2211420.
[4] H. Seo, L. Jeon, J. Kwon, H. Lee, *Adv. Healthcare Mater.* **2023**, *12*, 2203033.
[5] L. Schoenmaker, D. Witzigmann, J. A. Kulkarni, R. Verbeke, G. F. A. Kersten, W. Jiskoot, D. J. A. Crommelin, *Int. J. Pharm.* **2021**, *601*, 120586.
[6] B. Matthias, B. Weber, H. Haas, P. Heller, S. Nogueira, A. Schlegel, RNA Particles Comprising Polysarcosine US Patent App. 17/281,697, **2022**.
[7] B. Weber, A. Birke, K. Fischer, M. Schmidt, M. Barz, *Macromolecules* **2018**, *51*, 2653.
[8] K. Klinker, O. Schäfer, D. Huesmann, T. Bauer, L. Capelôa, L. Braun, N. Stergiou, M. Schinnerer, A. Dirisala, K. Miyata, *Angew. Chem.* **2017**, *56*, 9608.
[9] Y. Hu, Y. Hou, H. Wang, H. Lu, *Bioconjug. Chem.* **2018**, *29*, 2232.
[10] F. Fenaroli, U. Repnik, Y. Xu, K. Johann, S. Van Herck, P. Dey, F. M. Skjeldal, D. M. Frei, S. Bagherifam, A. Kocere, R. Haag, B. G. De Geest, M. Barz, D. G. Russell, G. Griffiths, *ACS Nano* **2018**, *12*, 8646.
[11] E. J. L. Steen, J. T. Jorgensen, K. Johann, K. Norregaard, B. Sohr, D. Svatunek, A. Birke, V. Shalgunov, P. E. Edem, R. Rossin, C. Seidl, F. Schmid, M. S. Robillard, J. L. Kristensen, H. Mikula, M. Barz, A. Kjaer, M. M. Herth, *ACS Nano* **2020**, *14*, 568.
[12] T. A. Bauer, J. Schramm, F. Fenaroli, S. Siemer, C. I. Seidl, C. Rosenauer, R. Bleul, R. Stauber, K. Koynov, M. Maskos, M. Barz, *Adv. Mater.* **2023**, *35*, 2210704.
[13] N. K. Dal, G. Schäfer, A. M. Thompson, S. Schmitt, N. Redinger, N. Alonso-Rodriguez, K. Johann, J. Ojong, J. Wohlmann, A. Best, K. Koynov, R. Zentel, U. E. Schable, G. Griffiths, M. Barz, F. Fenaroli, J. Controlled Release, (Eds: J. W. Goodby, P. J. Collings, T. Kato, C. Tschierske, H. Gleeson, P. Raynes, V. Vill), **2023**, *354*, 851.
[14] C. Kappel, C. Seidl, C. Medina-Montano, M. Schinnerer, I. Alberg, C. Leps, J. Sohl, A. K. Hartmann, M. Fichter, M. Kuske, J. Schunke, G. Kuhn, I. Tubbe, D. Paßlick, D. Hobernik, R. Bent, K. Haas, E. Montermann, K. Walzer, M. Diken, M. Schmidt, R. Zentel, L. Nuhn, H. Schild, S. Tenzer, V. Mailänder, M. Barz, M. Bros, S. Grabbe, *ACS Nano* **2021**, *15*, 15191.
[15] I. Alberg, S. Kramer, M. Schinnerer, Q. Hu, C. Seidl, C. Leps, N. Drude, D. Möckel, C. Rijcken, T. Lammers, M. Diken, M. Maskos, S. Morsbach, K. Landfester, S. Tenzer, M. Barz, R. Zentel, *Small* **2020**, *16*, 1907574.
[16] I. Negwer, A. Best, M. Schinnerer, O. Schäfer, L. Capeloa, M. Wagner, M. Schmidt, V. Mailänder, M. Helm, M. Barz, H.-J. Butt, K. Koynov, *Nat. Commun.* **2018**, *9*, 5306.
[17] B. Weber, C. Seidl, D. Schwiertz, M. Scherer, S. Bleher, R. Süss, M. Barz, *Polymers* **2016**, *8*, 427.
[18] C. Muhl, M. Conrad, D. Unthan, M. Barz, *Eur. Polym. J.* **2019**, *120*, 109223.
[19] S. Bleher, J. Buck, C. Muhl, S. Sieber, S. Barnert, D. Witzigmann, J. Huwyler, M. Barz, R. Süss, *Small* **2019**, *15*, 1904716.
[20] K. Son, M. Ueda, K. Taguchi, T. Maruyama, S. Takeoka, Y. Ito, *J. Controlled Release* **2020**, *322*, 209.
[21] S. S. Nogueira, A. Schlegel, K. Maxeiner, B. Weber, M. Barz, M. A. Schroer, C. E. Blanchet, D. I. Svergun, S. Ramishetti, D. Peer, P. Langguth, U. Sahin, H. Haas, *ACS Appl. Nano Mater.* **2020**, *3*, 10634.
[22] C. Wilhelmy, I. S. Keil, L. Uebbing, M. A. Schroer, D. Franke, T. Nawroth, M. Barz, U. Sahin, H. Haas, M. Diken, P. Langguth, *Pharmaceutics* **2023**, *15*, 2068.
[23] L. Capelôa, M. Yazdi, H. Zhang, X. Chen, Y. Nie, E. Wagner, U. Lächelt, M. Barz, *Macromol. Rapid Commun.* **2022**, *43*, 2100698.
[24] D. Bi, D. M. Unthan, L. Hu, J. Bussmann, K. Remaut, M. Barz, H. Zhang, *J. Controlled Release* **2023**, *356*, 1.
[25] Q. Cheng, T. Wei, L. Farbiak, L. T. Johnson, S. A. Dilliard, D. J. Siegwart, *Nat. Nanotechnol.* **2020**, *15*, 313.
[26] C. B. Roces, G. Lou, N. Jain, S. Abraham, A. Thomas, G. W. Halbert, Y. Perrie, *Pharmaceutics* **2020**, *12*, 1095.
[27] M. Maeki, S. Uno, A. Niwa, Y. Okada, M. Tokeshi, *J. Controlled Release* **2022**, *344*, 80.
[28] M. Maeki, T. Saito, Y. Sato, T. Yasui, N. Kaji, A. Ishida, H. Tani, Y. Baba, H. Harashima, M. Tokeshi, *RSC Adv.* **2015**, *5*, 46181.
[29] N. Kimura, M. Maeki, A. Ishida, H. Tani, M. Tokeshi, *ACS Appl. Bio. Mater.* **2021**, *4*, 1783.
[30] M. Maeki, Y. Fujishima, Y. Sato, T. Yasui, N. Kaji, A. Ishida, H. Tani, Y. Baba, H. Harashima, M. Tokeshi, *PLoS One* **2017**, *12*, 0187962.
[31] C. Webb, N. Forbes, C. B. Roces, G. Anderluzzi, G. Lou, S. Abraham, L. Ingalls, K. Marshall, T. J. Leaver, J. A. Watts, J. W. Aylott, Y. Perrie, *Int. J. Pharm.* **2020**, *582*, 119266.
[32] N. Kimura, M. Maeki, Y. Sato, Y. Note, A. Ishida, H. Tani, H. Harashima, M. Tokeshi, *ACS Omega* **2018**, *3*, 5044.
[33] N. Kimura, M. Maeki, Y. Sato, A. Ishida, H. Tani, H. Harashima, M. Tokeshi, *ACS Appl. Mater. Interfaces* **2020**, *12*, 34011.
[34] N. Kimura, M. Maeki, K. Sasaki, Y. Sato, A. Ishida, H. Tani, H. Harashima, M. Tokeshi, *RSC Adv.* **2021**, *11*, 1430.
[35] S. Q. Zheng, E. Palovcak, J.-P. Armache, K. A. Verba, Y. Cheng, D. A. Agard, *Nat. Methods* **2017**, *14*, 331.
[36] C. E. Blanchet, A. Spilotros, F. Schwemmer, M. A. Graewert, A. Kikhney, C. M. Jeffries, D. Franke, D. Mark, R. Zengerle, F. Cipriani, S. Fiedler, M. Roesslea, D. I. Svergun, *J. Appl. Crystallogr.* **2015**, *48*, 431.
[37] A. Round, F. Felisaz, L. Fodinger, A. Gobbo, J. Huet, C. Villard, C. E. Blanchet, P. Pernot, S. McSweeney, M. Roessle, D. I. Svergun, F. Cipriani, *Acta Crystallogr., D* **2015**, *71*, 67.
[38] K. Manalastas-Cantos, P. V. Konarev, N. R. Hajizadeh, A. G. Kikhney, M. V. Petoukhov, D. S. Molodenskiy, A. Panjkovich, H. D. T. Mertens, A. Gruzinov, C. Borges, C. M. Jeffries, D. I. Svergun, D. Franke, *J. Appl. Crystallogr.* **2021**, *54*, 343.
[39] D. Franke, A. G. Kikhney, D. I. Svergun, *Nucl. Instrum. Methods Phys. Res. A* **2012**, *689*, 52.
[40] K. A. Rubinson, C. Stanley, S. Krueger, *J. Appl. Crystallogr.* **2008**, *41*, 456.
[41] A. Guinier, *Ann. Phys.* **1939**, *11*, 161.
[42] S. Ciccariello, J. Goodisman, H. Brumberger, *J. Appl. Crystallogr.* **1988**, *21*, 117.
[43] W. H. Bragg, W. L. Bragg, *Proc. R. Soc. London Ser., A* **1913**, *88*, 428.
[44] *Handbook of Liquid Crystals* (Eds: J. W. Goodby, P. J. Collings, T. Kato, C. Tschierske, H. Gleeson, P. Raynes, V. Vill), Wiley-VCH, Weinheim, Germany **2014**.
[45] D. D. Kang, X. Hou, L. Wang, Y. Xue, H. Li, Y. Zhong, S. Wang, B. Deng, D. W. McComb, Y. Dong, *Bioact. Mater.* **2024**, *37*, 86.
[46] C. Hald Albertsen, J. A. Kulkarni, D. Witzigmann, M. Lind, K. Petersson, J. B. Simonsen, *Adv. Drug Delivery Rev.* **2022**, *188*, 114416.

[47] M. Cárdenas, R. A. Campbell, M. Yanez Arteta, M. J. Lawrence, F. Sebastiani, *Curr. Opin. Colloid Interface Sci.* **2023**, *66*, 101705.
[48] Y. Eygeris, S. Patel, A. Jozic, G. Sahay, *Nano Lett.* **2020**, *20*, 4543.
[49] M. A. Graewert, C. Wilhelmy, T. Bacic, J. Schumacher, C. Blanchet, F. Meier, R. Drexel, R. Welz, B. Kolb, K. Bartels, T. Nawroth, T. Klein, D. Svergun, P. Langguth, H. Haas, *Sci. Rep.* **2023**, *13*, 15764.
[50] C. D. Siewert, H. Haas, V. Cornet, S. S. Nogueira, T. Nawroth, L. Uebbing, A. Ziller, J. Al-Gousous, A. Radulescu, M. A. Schroer, C. E. Blanchet, D. I. Svergun, M. P. Radsak, U. Sahin, P. Langguth, *Cells* **2020**, *9*, 2034.
[51] A. G. Hadjigeorgiou, A. G. Boudouvis, G. Kokkoris, *Chem. Eng. J.* **2021**, *414*, 128775.
[52] P. Patel, N. M. Ibrahim, K. Cheng, *Trends Pharmacol. Sci.* **2021**, *42*, 448.
[53] Z. He, Y. Hu, T. Nie, H. Tang, J. Zhu, K. Chen, L. Liu, K. W. Leong, Y. Chen, H.-Q. Mao, *Acta Biomater.* **2018**, *81*, 195.
[54] D. Chen, K. T. Love, Y. Chen, A. A. Eltoukhy, C. Kastrup, G. Sahay, A. Jeon, Y. Dong, K. A. Whitehead, D. G. Anderson, *J. Am. Chem. Soc.* **2012**, *134*, 6948.
[55] S. Wang, X. Wei, X. Sun, C. Chen, J. Zhou, G. Zhang, H. Wu, B. Guo, L. Wei, *Int. J. Nanomed.* **2018**, *13*, 617.
[56] M. H. Y. Cheng, J. Leung, Y. Zhang, C. Strong, G. Basha, A. Momeni, Y. Chen, E. Jan, A. Abdolahzadeh, X. Wang, J. A. Kulkarni, D. Witzigmann, P. R. Cullis, *Adv. Mater.* **2023**, *35*, 2303370.
[57] A. K. K. Leung, Y. Y. C. Tam, S. Chen, I. M. Hafez, P. R. Cullis, *J. Phys. Chem. B* **2015**, *119*, 8698.
[58] M. Y. Arteta, T. Kjellman, S. Bartesaghi, S. Wallin, X. Wu, A. J. Kvist, A. Dabkowska, N. Székely, A. Radulescu, J. Bergenholtz, L. Lindfors, *Proc. Natl. Acad. Sci. USA* **2018**, *115*, E3351.
[59] K. J. Hassett, J. Higgins, A. Woods, B. Levy, Y. Xia, C. J. Hsiao, E. Acosta, Ö. Almarsson, M. J. Moore, L. A. Brito, *J. Controlled Release* **2021**, *335*, 237.
[60] M. Kawaguchi, M. Noda, A. Ono, M. Kamiya, M. Matsumoto, M. Tsurumaru, S. Mizukami, H. Mukai, S. Kawakami, *J. Pharm. Sci.* **2023**, *112*, 1401.
[61] D. Orthaber, A. Bergmann, O. Glatter, *J. Appl. Crystallogr.* **2000**, *33*, 218.
[62] S. Patel, N. Ashwanikumar, E. Robinson, Y. Xia, C. Mihai, J. P. Griffith 3rd, S. Hou, A. A. Esposito, T. Ketova, K. Welsher, K. Welsher, J. L. Joyal, Ö. Almarsson, G. Sahay, *Nat. Commun.* **2020**, *11*, 983.
[63] F. Campbell, F. L. Bos, S. Sieber, G. Arias-Alpizar, B. E. Koch, J. Huwyler, A. Kros, J. Bussmann, *ACS Nano* **2018**, *12*, 2138.